



Detection of Alzheimer's disease using features of brain region-of-interest-based individual network constructed with the sMRI image

Jinwang Feng^a, Shao-Wu Zhang^{a,*}, Luonan Chen^{a,b,c,d,*}, Chunman Zuo^b, for the Alzheimer's Disease Neuroimaging Initiative¹

^a Key Laboratory of Information Fusion Technology of Ministry of Education, School of Automation, Northwestern Polytechnical University, Xi'an 710072, China

^b Key Laboratory of Systems Biology, Shanghai Institutes of Biochemistry and Cell Biology, Center for Excellence in Molecular Science, Chinese Academy of Sciences, Shanghai 200031, China

^c Key Laboratory of Systems Biology, Hangzhou Institute for Advanced Study, University of Chinese Academy of Sciences, Chinese Academy of Sciences, Hangzhou 310024, China

^d School of Life Science and Technology, ShanghaiTech University, Shanghai 201210, China

ARTICLE INFO

Keywords:

Alzheimer's disease detection
Magnetic resonance imaging
Shearlet transform
Brain network
Energy feature extraction

ABSTRACT

Brain networks constructed with regions of interest (ROIs) from the structural magnetic resonance imaging (sMRI) image are widely investigated for detecting Alzheimer's disease (AD). However, the ROI is generally represented by spatial domain-based features, so attentions are hardly paid to constructing a brain network with the frequency domain-based feature. In order to accurately characterize the ROI in the frequency domain and then construct an individual network, in this study, a novel method, which can describe the ROI properly by directional subbands and capture correlations between those ROIs, is proposed to construct a shearlet subband energy feature-based individual network (SSBIN) for AD detection. Specifically, the SSBIN is constructed with 90 ROIs which are segmented from the pre-processed sMRI image based on the automated anatomical labeling atlas, the 90 ROIs are represented by directional subband-based energy feature vectors (SVs) formed by jointing energy features extracted from their directional subbands, and the weight values of the SSBIN are computed by Pearson's correlation coefficient (PCC). Subsequently, two network features are extracted from the SSBIN: the node feature vector (NV) is computed by averaging the 90 SVs; the low dimensional edge feature vector (LV) is obtained by kernel principal component analysis (KPCA). Following that the concatenation of NV and LV is used as a SSBIN-based feature for the sMRI image. Finally, we use support vector machine (SVM) with the radial basis function kernel as classifier to categorize 680 subjects selected from the AD Neuroimaging Initiative (ADNI) database. Experimental results validate that the ROI can be properly characterized by the NV, and correlations between ROIs captured by the LV play an important role in AD detection. Besides, a series of comparisons with four current state-of-the-art approaches demonstrate the higher AD detecting performance of the SSBIN method.

1. Introduction

As the most complicated network, a healthy human brain is consisted of about 100 billion of neurons, and these neurons also have complex connections between their long and branching extensions (Dai and Guo, 2017; Liu et al., 2015). Studies have suggested that broken connections between those neurons are the main reasons causing most brain

diseases, such as Alzheimer's disease (AD) and its prodromal stage-mild cognitive impairment(MCI), which has been testified by many recently published works (Moetesum et al., 2019; Zhou et al., 2020; El-Yacoubi et al., 2019; Zhang et al., 2020, 2019).

Nowadays, Alzheimer is still not a curable neuro-degenerative disease, which is also gradually progressive with aging. Hence, it leads to be a main type for dementia with age more than 65 years. For example,

* Corresponding authors at: Key Laboratory of Information Fusion Technology of Ministry of Education, School of Automation, Northwestern Polytechnical University, Xi'an 710072, China

E-mail addresses: zhangsw@nwpu.edu.cn (S.-W. Zhang), lnchen@sibs.ac.cn (L. Chen).

¹ Data used in this article are obtained from the ADNI database. For more information, we refer readers to website of the ADNI: adni.loni.usc.edu.

the year 2006 witnessed more than 26 million people with AD worldwide, and by 2050, one among 85 people will be affected by AD (Stefano et al., 2019); Total payments, in 2008, for all kinds of services to dementia people age > 65 years, are predicted to be \$277 billion in USA (Alzheimer's Association, 2018). Researches had revealed that with aging, the MCI patient's and the healthy control (HC) individual's rates converting to AD highly reach to 15% and 2% per year, respectively; Obviously, the conversion rate for the MCI is higher than that of the HC (Ardekani et al., 2017; Thung et al., 2018). Besides, early detection for people with AD, estimated by a mathematical model, can save the medical and care cost up to \$7.9 trillion (Alzheimer's Association, 2018), which means that the early and accurate detection can make the AD patient benefit from his treatment and finance.

In clinical, under the help of the brain imaging equipment and technology, brain diseases, such as gray matter atrophies of the AD and MCI patients, can be clearly reflected and observed by their brain imaging (Coronado-Leija et al., 2017; Guo et al., 2017; Suk et al., 2015; Long et al., 2017; Wang et al., 2017). But it is impractical for clinicians to quickly detect MCI and AD patients from HC individuals when facing huge data produced by dementia patients. Therefore, researchers have made many efforts to characterize brain atrophy patterns related to AD, and then extract different kinds of features from the sMRI image to develop an accurate imaging marker for AD detection (Liu et al., 2018; Zhang et al., 2017; Cheng et al., 2019; Peng et al., 2019; Arbabshirani et al., 2017). Based on the techniques used to extract features from the sMRI image, we roughly divide the existing methods for AD detection into two categories: the spatial domain-based approach (Farrar et al., 2018; Vogel et al., 2018; Saravanakumar and Thangaraj, 2019; Cao et al., 2017; Beheshti et al., 2016) and the frequency domain-based approach (Zhang et al., 2018; Jha et al., 2018).

For the spatial domain-based method, features used for AD detection are directly extracted from the sMRI image by describing microstructural patterns of the atrophies (Ou et al., 2015; Partovi et al., 2017; Cevik et al., 2017; Giuletta et al., 2018; Glozman et al., 2017; Feng et al., 2016), or from a network constructed with different brain regions (Lu et al., 2018; Duraisamy et al., 2019; Wiepert et al., 2017; Swietlik and Bialowas, 2019). For example, Li et al. (2019) proposed to use a deep learning method together with the hippocampal MRI data for AD classification; Ju et al. (2019) proposed to put brain network and clinical relevant text information into a deep learning model for making early AD diagnosis; Liu et al. (2018) extracted features from a developed hierarchical network of the brain for detecting AD, and they also proposed to use a brain network's edge and node features for classifying AD patient (Liu et al., 2017). It is well known that a sMRI image consists of millions of voxels, which makes the spatial domain-based method poorer in the issue of reducing dimensionality. The reason is that a high dimensional spatial feature is extracted to characterize the atrophy patterns related to AD precisely and describe the sMRI image well, but it will lead to a poor performance for the classifier when using this kind of feature to make a decision.

For the frequency domain-based method, features for detecting AD are indirectly extracted from the sMRI image by capturing energy distribution patterns of the brain atrophies reflected in the directional subbands at different scales. For example, Zhang et al. (2018) extracted features from an MRI based on stationary wavelet entropy for AD classification; Jha et al. (2018) developed a novel computer-aided diagnosis cascade model using the dual-tree complex wavelet transform to categorize AD patients; Feng et al. (2020) used wavelet transformation energy feature of the sMRI image for AD identification; In their another work (Feng et al., 2021), a subband network constructed with the non subband contourlet transform was used for AD classification. However, the frequency domain-based feature is an overall representation for the sMRI image, which makes its interpretability poor; Furthermore, correlations between different brain ROIs are also neglected in this kind of feature. The reason is that before feature extraction, transformation, such as wavelet (Dong et al., 2017) or contourlet (Do and Vetterli, 2005;

Cunha et al., 2006), firstly perform on the sMRI image.

In order to construct a brain ROI-based individual network in the frequency domain with the ROI's energy features and then extract low-dimensional features from the sMRI image, in this study, a novel method is proposed to construct a shearlet subband energy feature-based individual network (SSBIN) for AD detection. Particularly, we firstly segment the pre-processed sMRI image into 90 ROIs based on the automated anatomical labeling (AAL) atlas (Tzourio-Mazoyer et al., 2002). And then we do the shearlet transform separately on each of the 90 ROIs to get their directional subbands at different scales, following that three energy features are computed based on each directional subband and a ROI is represented by a SV which is formed by jointing energy features of the ROI's directional subbands. Subsequently, the SSBIN is constructed with the 90 SVs, and is weighted by PCC. We then extract two features from the SSBIN, the NV is computed by averaging the 90 SVs, and the LV is obtained by KPCA. Finally, the concatenation of NV and LV is regarded as a SSBIN-based feature of the sMRI image. Meanwhile, we use SVM with the radial basis function (RBF) kernel as classifier for AD detection. Experimental results validate that the ROI can be properly depicted by the NV, and correlations between ROIs captured by the LV are of importance for detecting AD. Besides, comprehensive comparisons with four other state-of-the-art approaches demonstrate the higher AD detecting performance of the SSBIN method under four metrics, which indicate that the SSBIN-based feature can be an assistant imaging marker for the clinical AD diagnosis.

In this study, our main contributions include three points. First, a novel method is proposed to construct a ROI-based individual brain network with the sMRI image in the frequency domain for AD detection. Second, instead of extracting spatial features directly from the brain ROI, the proposed SSBIN method uses shearlet to transform the ROI into directional subbands firstly, and then extract energy features from the subbands to represent the ROI. Third, the proposed SSBIN method describe the sMRI image in the frequency domain, while construct brain network in the spatial domain, which ensures that the SSBIN-based feature has a low dimensionality and contains the advantages of both the spatial domain and the frequency domain.

The rest of this work is organized as follows. Materials and methods are given in Section 2. Experimental metrics and results are introduced in Section 3. Comparisons with four state-of-the-art approaches are shown in Section 4. Finally, a brief conclusion to this study is provided in Section 5.

2. Materials and methods

In this section, materials used in this study and their pre-processing are firstly introduced, and then we show the proposed method of how to construct the shearlet subband energy feature-based individual network (SSBIN) in detail.

2.1. Materials

The ADNI was launched in 2003, and its primary goal is to measure the progression of MCI and early AD using brain imaging, and other clinical information. For more information, we refer readers to website of the ADNI: adni.loni.usc.edu. We select 680 samples from the ADNI database, including 200 AD, 280 MCI and 200 HC. Among the 280 MCI subjects, 120 samples who will convert to AD in the follow-up are denoted as MCIC; the remaining is denoted as MCInc. We use the 680 sMRI images to construct AD-vs-HC, ADvs-MCI, MCI-vs-HC, MCIC-vs-MCInc four data sets. Table 1 provides more detail demographic information about the 680 selected subjects.

Before extracting feature from the 680 sMRI images, we perform motion correction, registration and skull strap, segmentation, and smoothing to them using statistic parametric mapping (SPM8) (Ashburner and Group, 1994) and voxel-based mapping (VBM8) (Ashburner and Friston, 2000) to remove uninformative brain tissues and make sure

Table 1

Demographic information of the 680 subjects selected from the ADNI database.

Type	Gender (F/M)	Number	Age (Mean±D)	MMSE (Mean±D)
AD	78/122	200	76.85±7.01	22.15±3.17
MCIc	67/53	120	78.65±9.73	26.38±3.76
MCIinc	71/89	160	73.59±7.68	26.21±2.67
MCI	138/142	280	75.76±8.96	26.28±3.17
HC	84/116	200	76.21±4.97	29.09±1.15

that different subjects' certain brain region is at the same position. After four preprocessing steps, the original sMRI image generates gray matter (GM), cerebrospinal fluid (CSF), and white matter (WM) three brain tissue images. Fig. 1 shows a visual comparison of the preprocessed and the original sMRI images, which is an example of four scans of the preprocessed and the raw sMRI images. Considering the fact that the GM image is mostly related to AD, so we select the GM image to extract the SSBIN-based feature, and then we will conduct experiments on AD-vs-HC, AD-vs-MCI, MCI-vs-HC and MCIc-vs-MCIinc four data sets to evaluate the AD detecting performance of the SSBIN method.

2.2. Method of extracting the SSBIN-based feature

Procedure of the automated anatomical labeling (AAL) atlas was provided by the Montreal Neurological Institute (Tzourio-Mazoyer et al., 2002). In this study, we use the interface under the SPM8 package to segment the GM image into 90 ROIs (Zhu et al., 2019; Cuingnet et al., 2011; Zhou et al., 2014). For convenience, those GM images are numbered and put into a set which is denoted as $\{GM^i\}_{i=1}^N$, here $N = 680$. After segmentation, 90 ROIs of the i -th GM image GM^i can be obtained $ROI_j^i, j = 1, 2, \dots, 90$. Obviously, the ROI segmented by AAL is a 3D image, but sizes of the 90 ROIs are different, and each ROI contains more redundancy than the useful information, such as the black background. Therefore, non-zero voxels contained in the 3D ROI are selected and then reshaped as a 2D image by column. In the following, the reshaped

2D image is also called as ROI. For brevity, we use a set, $\{ROI_j^i\}$, to represent ROIs of the N GM images, here $j(j = 1, 2, \dots, 90)$ is the j -th ROI of the i -th GM image.

It has been widely acknowledged that traditional wavelets are not very effective in dealing signals containing distributed discontinuities (Easley et al., 2008). To overcome this limitation, the shearlet transform was developed to capture the intrinsic geometrical features. The shearlet is by means of a simple but rigorous mathematical framework which provides a more flexible theoretical tool for the geometrical representation of multidimensional data (Dong et al., 2015). Considering advantages of the shearlet (Feng et al., 2016), we will decompose the ROI by shearlet. Given the j -th ROI of the i -th GM image, ROI_j^i , it is decomposed by the shearlet with S directional levels and L decomposition scales, and we can obtain $(2^S + 2) \times L$ directional subbands and a low frequency subband. Fig. 2 shows the decomposition of a ROI by the shearlet with one directional level and two decomposition scales, so there are $(2^1 + 2) \times 2 = 8$ high frequency subbands and a low frequency subband. It can be seen from Fig. 2 that the low frequency subband only contains macro-structural information which is not related to AD; hence the low frequency subband is abandoned in the SSBIN method. For brevity, a set is used to contain and number the directional subbands of the 90 ROIs, which is denoted as $\{SB_{j,k}^i\}$, here $i(i = 1, 2, \dots, N)$ is the i -th GM image, $j(j = 1, 2, \dots, 90)$ is the j -th ROI of the i -th GM image, and $k(k = 1, 2, \dots, (2^S + 2) \times L)$ is the k -th directional subband of the j -th ROI of the i -th GM image.

Coefficients with different modulus in a directional subband describe the energy distribution of the spatial structures in the frequency domain. To precisely represent the directional subband, three energy features are computed to capture different energy distribution patterns in the directional subband, which are separately represented by

$$e1 = \frac{1}{M} \sum_{x=1}^M |SB(x)| \quad (1)$$

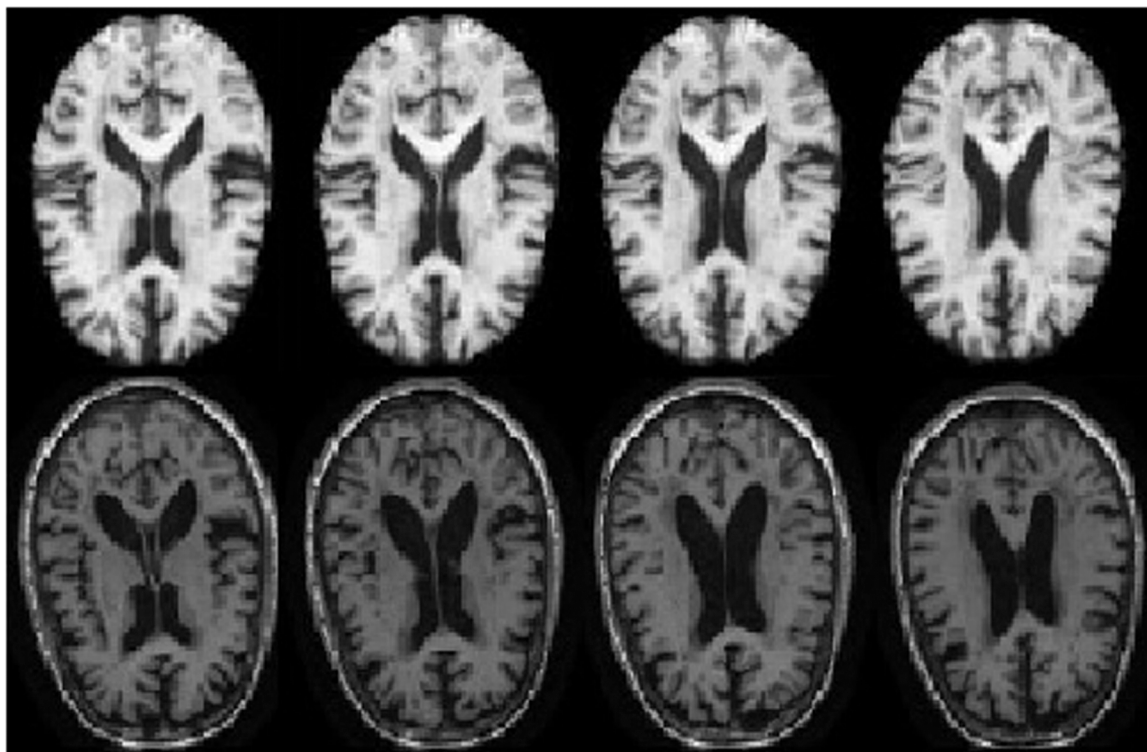


Fig. 1. An example of four scans from the preprocessed (first column) and the raw (second column) sMRI images.

Table 2
The pseudo-code of extracting the SSBIN feature from the GM image.

Input: the GM image	Output: the SSBIN feature
1. Segment the GM image into 90 ROIs based on AAL: $ROI_j, j = 1, 2, \dots, 90$.	
2. While $j \leq 90$	
3. Doing shearlet transform on ROI_j to get its subbands	
4. Computing SV_j of the ROI_j based on Eqs. (1), (2), (3), (4) and (5)	
5. $j = j + 1$	
6. End	
7. Constructing SSBIN of the GM image based on 90 SVs and Eq. (6)	
8. Return the SSBIN feature extracted from the SSBIN	

basis function (RBF) as the kernel of the SVM classifier, which is formulated as

$$k(SSBIN^1, SSBIN^2) = \exp\left(-\frac{\|SSBIN^1 - SSBIN^2\|^2}{2\sigma^2}\right) \quad (12)$$

Obviously, regarding to the SVM classifier with RBF kernel, two important parameters, the window width of the RBF kernel σ and the penalty coefficient of the SVM classifier C , need be estimated based on experiments. The σ determines the number of support vectors, and the C can control the penalty degree for error. Therefore, σ and C should be estimated based on experiments carefully.

In short, in order to accurately characterize the ROI in the frequency

domain and then construct an individual network, the pre-processed sMRI image is firstly divided into 90 ROIs using the AAL atlas. Then the shearlet transform is separately performed on each of these ROIs, following that a ROI is represented by the SV. Subsequently, a SSBIN is constructed with the 90 SVs and is weighted by PCC. Finally, NV of the SSBIN is computed by averaging these SVs, LV of the SSBIN is computed by KPCA, and concatenation of the NV and the LV is regarded as a SSBIN-based feature, which is used as input of the SVM classifier for AD detection. Fig. 4 shows the flowchart of the SSBIN method.

3. Experimental metrics and results

In this section, multiple experiments are conducted to evaluate the AD detecting performance of the SSBIN method on AD-vs-HC, AD-vs-MCI, MCI-vs-HC, MCIc-vs-MCIc data sets. We firstly introduce experimental metrics used in this study, and followed by experimental results of the SSBIN method.

3.1. Metrics

For each of the four data sets, samples are randomly divided into ten subsets, nine of them are used for training, and the rest is used for test. The above process is randomly done ten times to get an unbiased estimation for the SSBIN method. Finally, we use mean classification ac-

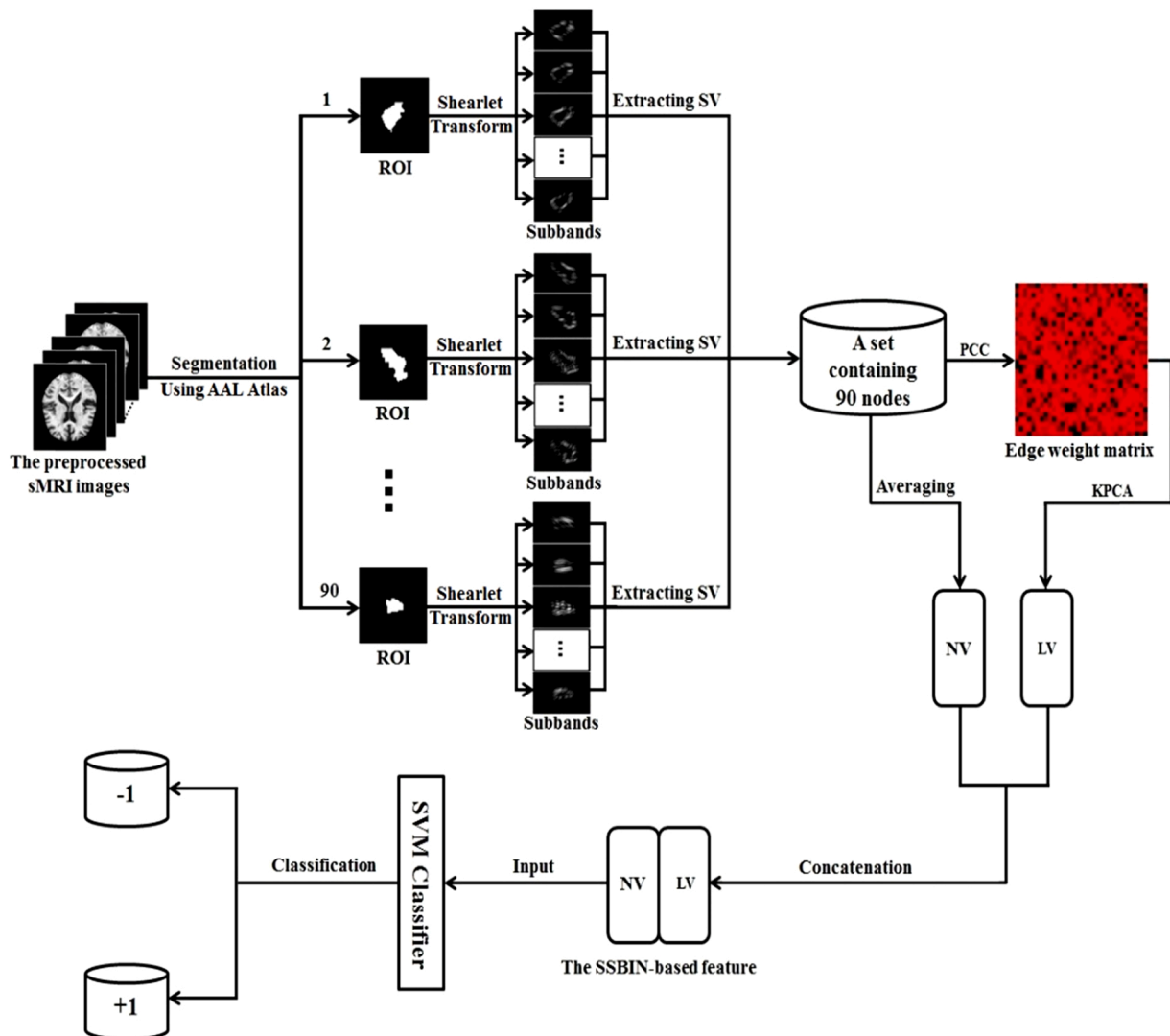


Fig. 4. Flowchart of the proposed method for AD Detection using features of the shearlet subband energy feature-based individual network.

curacy (MC_ACC), mean classification sensitivity (MC_Se), mean classification specificity (MC_Sp), and area under the receiver operating characteristic curve (AUC) of the ten experiments as the final results on a data set. The MC_ACC, MC_Se, and MC_Sp are separately formulated as

$$MC_ACC = \frac{1}{10} \sum_{i=1}^{10} \frac{TP_i + TN_i}{TP_i + FP_i + TN_i + FN_i} \quad (13)$$

$$MC_Se = \frac{TP_i}{TP_i + FN_i} \quad (14)$$

and

$$MC_Sp = \frac{TN_i}{FP_i + TN_i} \quad (15)$$

where TP_i is the number of correctly classified positive subjects, FP_i is the number of incorrectly classified positive subjects, TN_i is the number of correctly classified negative subjects, FN_i is the number of incorrectly classified negative subjects, and i ($i = 1, 2, \dots, 10$) is the i -th experiment on a data set.

3.2. Results

For the shearlet transform, the directional factor S and the decomposition scale L determine the number of subbands for each ROI, which indirectly affect the SV's structural stability. Therefore, we do multiple experiments on AD-vs-HC, AD-vs-MCI, MCI-vs-HC, and MCIc-vs-MCIc data sets to obtain an optimal combination between S and L . Fig. 5 shows MC_ACCs of experiments with different S and L values on the four data sets. It can be obviously seen from Fig. 5 that when $S \leq 3$, MC_ACCs on the four data sets gradually increase, while after $S > 3$, MC_ACCs drastically decrease, and meanwhile MC_ACCs of the experiments with $L = 1$ on the four data sets are better than those of experiments with $L > 1$. In terms of MC_ACCs shown in Fig. 5, we set $S = 3$ and $L = 1$ as the

optimal parameters of the shearlet transform. As a result, a ROI is decomposed into $(2^S + 2) \times L = 10$ directional subbands, and the dimensionality of the SV is $3 \times (2^S + 2) \times L = 30$, that is, nodes (NV) of the SSBIN are represented by a 1×30 vector.

For the KPCA with a Gaussian kernel, the number of principal components P (namely, the dimensionality of LV) and the width of the Gaussian Kernel K_W are needed to be estimated by AD detecting experiments. MC ACCs of experiments with different P and K_W values on AD-vs-HC, AD-vs-MCI, MCI-vs-HC, and MCIc-vs-MCIc data sets are given in Fig. 6. According to Fig. 6(a), we can find that the best MC ACC falls in the interval $15 < P < 25$. In order to obtain the optimal estimation P value, we further perform experiments when $15 < P < 25$, and MC ACCs are shown in Fig. 6(b). We can see from Fig. 6(b) that with the increase of P , MC ACCs of the SSBIN method also gradually increase; After $P > 19$, MC ACCs begin to decrease gradually. Therefore, we set $P = 19$. Similarly, according to Fig. 6(c), we can find that when $1.0 < K_W < 2.0$, the best MC ACC of the SSBIN method can be achieved. In order to obtain the optimal estimation K_W value, we also further conduct experiments when $1.0 < K_W < 2.0$, and MC ACCs are shown in Fig. 6(d). Based on Fig. 6(d), we can see that with the increase of K_W , MC ACCs of the SSBIN method gradually increase; After $K_W > 1.3$, MC ACCs of the SSBIN method start to decrease gradually. Hence we set $K_W = 1.3$. In terms of MC ACCs shown in Fig. 6, we set $P = 19$ and $K_W = 1.3$ as the optimal estimation parameters of the KPCA in this study. It can be obviously found that the final dimensionality of the SSBIN-based feature is $3 \times (2^S + 2) \times L + P = 49$.

To explain why the KPCA with the Gaussian kernel is used in this method, experiments under the PCA and the KPCA with linear (KPCA-L), polynomial (KPCA-P), and Gaussian (KPCA-G) kernels are performed on AD-vs-HC, AD-vs-MCI, MCI-vs-HC, and MCIc-vs-MCIc data sets, and MC ACCs are shown in Fig. 7. It can be obviously seen from Fig. 7 that MC_ACCs, MC_Ses, and MC_Sps of the KPCA-G consistently outperform those of the other kernels, except for MC_Se of the KPCA-G on the MCI-

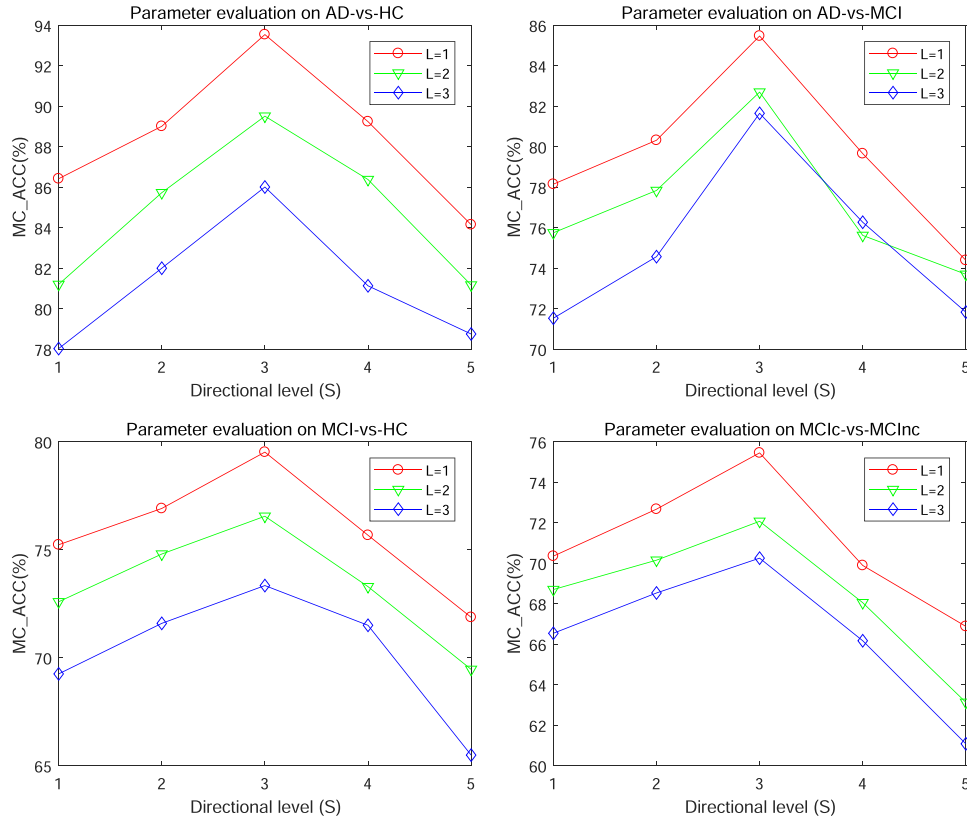


Fig. 5. MC ACCs of parameter estimation experiments with different S and L values on AD-vs-HC, AD-vs-MCI, MCI-vs-HC, and MCIc-vs-MCIc data sets.

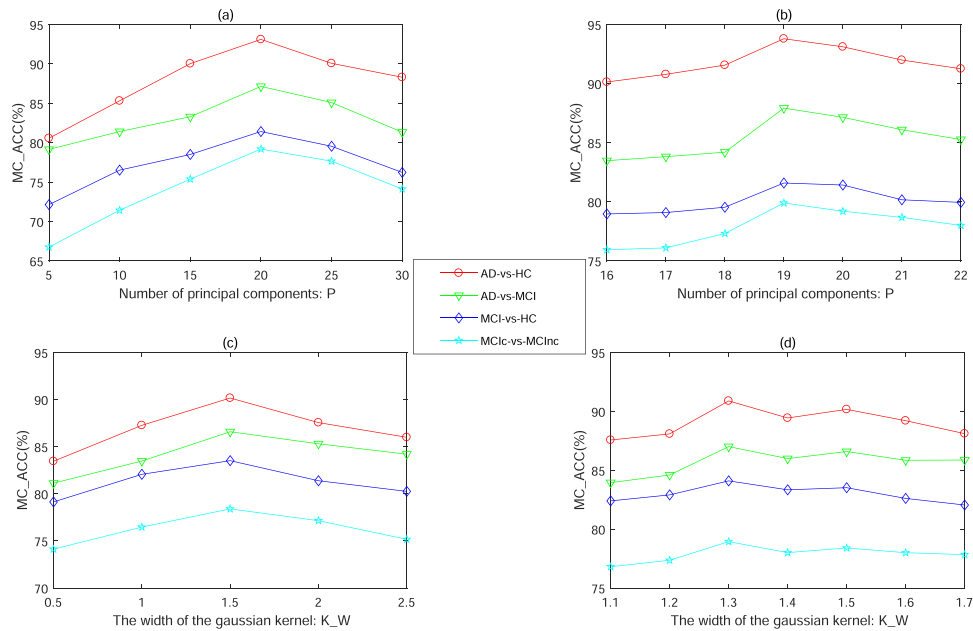


Fig. 6. MC_ACCs of parameter evaluation experiments for the KPCA with a Gaussian kernel on AD-vs-HC, AD-vs-MCI, MCI-vs-HC, and MCIc-vs-MCIc data sets. (a) and (b) MC ACCs of parameter evaluation experiments with different P values. (c) and (d) MC_ACCs of parameter evaluation experiments with different K_W values.

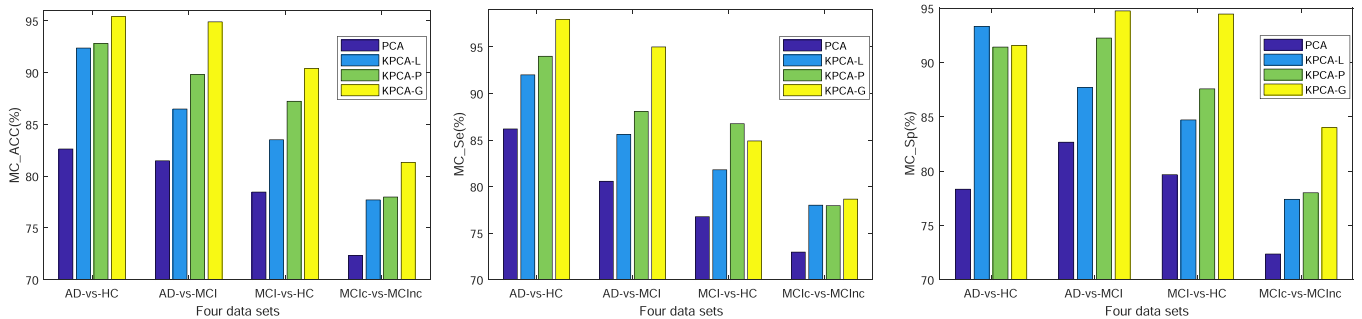


Fig. 7. Results of experiments under the PCA and the KPCA with linear (KPCA-L), polynomial (KPCA-P), and Gaussian (KPCA-G) kernels on AD-vs-HC, AD-vs-MCI, MCI-vs-HC, and MCIc-vs-MCIc data sets.

vs-HC data set which is inferior to that of the KPCA-P. The phenomenon shown in Fig. 7 indicates that correlations between different ROIs are not linear and the nonlinearity between these ROIs can be captured by KPCA with the Gaussian kernel in higher dimensional space. Hence, we select the KPCA with the Gaussian kernel to reduce the dimensionality of the SSBIN-based feature in this study.

For the SVM classifier with a RBF kernel, the window width of the RBF kernel σ and the penalty coefficient of the SVM classifier C are needed to be estimated by experiments to obtain their optimal values. We perform parameter estimation experiments for the SVM classifier with a RBF kernel on AD-vs-HC, AD-vs-MCI, MCI-vs-HC, and MCIc-vs-MCIc data sets, and MC_ACCs of the parameter estimation experiments with different σ and C values are given in Fig. 8. According to Fig. 8(a), we can find that the best MC ACC of the SSBIN-based feature falls in the interval $1.4 < \sigma < 2.8$. In order to get the optimal estimation σ value, we do experiments when $1.9 < \sigma < 2.5$, and Fig. 8(b) shows experimental MC_ACCs. Based on Fig. 8(b), we can see that with the increase of σ , MC_ACCs of the SSBIN-based feature increase gradually, after $\sigma > 2.2$, MC_ACCs of the SSBIN-based feature begin to stabilize gradually. Therefore, we set $\sigma = 2.2$ as the optimal estimation value of the RBF kernel's window width. Similarly, according to Fig. 8(c), we can find that the best MC_ACC of the SSBIN-based feature can be achieved when $1 < C < 7$. In order to obtain the optimal estimation C value, another experiments are performed when $1 < C \leq 6$, and MC_ACCs are

shown in Fig. 8(d). Based on Fig. 8(d), we can see that with the increase of C , MC_ACCs of the SSBIN-based feature also gradually increase before $C \leq 2$, however, after $C > 2$, MC_ACCs of the SSBIN-based feature start to be stable gradually. Hence, we set $C = 2$ as the optimal estimation value of the SVM classifier's penalty coefficient. In terms of MC_ACCs shown in Fig. 8, we set $\sigma = 2.2$ and $C = 2$ as the optimal estimation parameters of the SVM classifier with the RBF kernel in this study.

Also, we further explore the influence of SVM with different kernel functions on the SSBIN-based feature in AD detection, AD detecting experiments using SVM with linear (SVM-L), quadratic (SVM-Q), polynomial (SVM-P), and RBF (SVM-RBF) kernels are performed on AD-vs-HC, AD-vs-MCI, MCI-vs-HC, and MCIc-vs-MCIc data sets, and experimental results are shown in Fig. 9. It can be obviously seen from Fig. 9 that MC_ACCs, MC_Ses, and MC_Sps of the SVM-RBF are consistently better than those of the others, except for MC Se of the SVM-RBF on the MCI-vs-HC data set which is inferior to those of the SVM-Q and SVM-P. The phenomenon shown in Fig. 9 indicates that the SSBIN-based feature is not linearly separable and the separability of the SSBIN-based features can be realized in high dimensional space by nonlinear classifier such as the SVM classifier with the RBF kernel. Therefore, we select the SVM classifier with the RBF kernel for AD detection in our SSBIN method.

For the SSBIN-based feature, it is made up of the edge feature LV and the node feature NV. We can confirm that the ROI and the correlation between different ROIs are two important information resources in

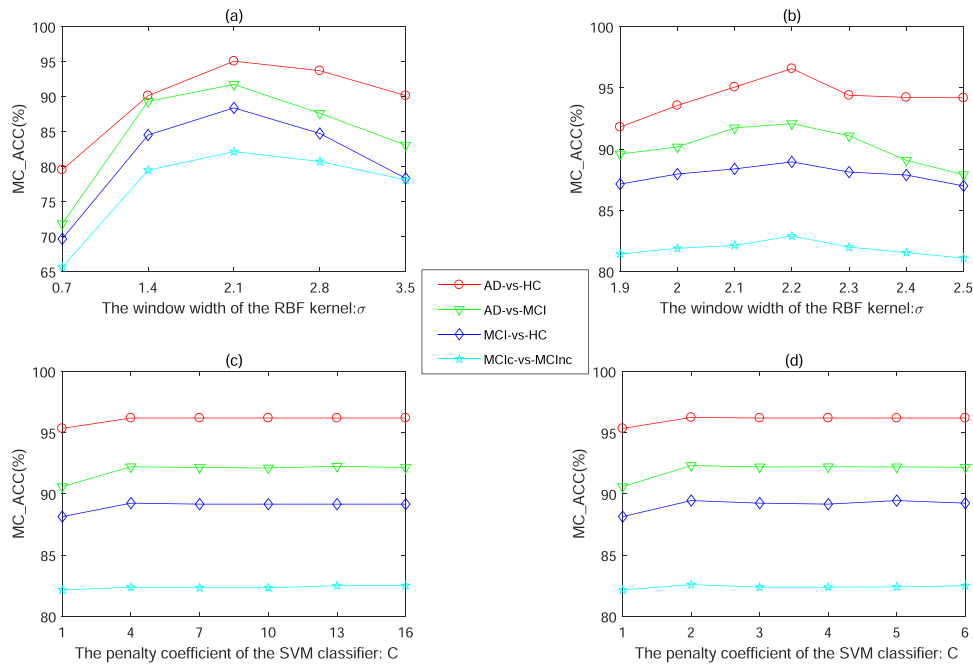


Fig. 8. MC_ACCs of parameter evaluation experiments for the SVM classifier with the Gaussian kernel on AD-vs-HC, AD-vs-MCI, MCI-vs-HC, and MCIc-vs-MCInc data sets. (a) and (b) MC_ACCs of different σ values. (c) and (d) MC_ACCs of different C values.

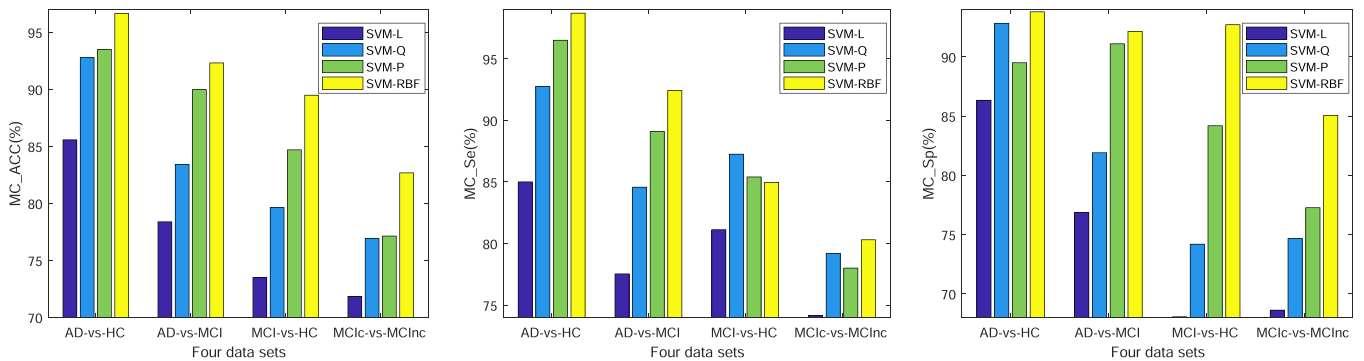


Fig. 9. Results of AD detecting experiments using the SVM classifier with linear (SVM-L), quadratic (SVM-Q), polynomial (SVM-P), and RBF (SVM-RBF) kernels on AD-vs-HC, AD-vs-MCI, MCI-vs-HC, and MCIc-vs-MCInc data sets.

sufficiently describing the sMRI image. But, we cannot tell which part is dominant for the SSBIN-based feature. To solve this issue, multiple AD detecting experiments using the LV, the NV and the SSBIN-based feature are performed on AD-vs-HC, AD-vs-MCI, MCI-vs-HC, and MCIc-vs-MCInc data sets under cases of the SVM classifier with linear (SVM-L), quadratic (SVM-Q), polynomial (SVM-P), and RBF (SVM-RBF) kernel functions. MC ACCs of the three features using the SVM with different kernel functions are shown in Fig. 10. It can be clearly found from Fig. 10 that on the four data sets, MC_ACCs of the SSBIN-based feature using SVM-L, SVM-Q, SVM-P, and SVM-RBF are consistently superior to those of the LV and the NV, and MC_ACCs of the LV with SVM-Q, SVM-P, and SVM-RBF obviously outperform those of the NV, while MC_ACCs of the NV using SVM-L are better than those of the LV. According to Fig. 10, we can conclude that features extracted from the ROI and the correlation between different ROIs can be complementary to each other, and in comparison with the NV, the LV has nonlinear separability in high dimensional space. In other words, the NV extracted from the directional subbands can accurately describe those abnormal energy distribution patterns in the ROI, correlations (edge weights) between different ROIs can be computed by PCC, and the LV extracted from these edge weights is properly reconstructed by the KPCA with the Gaussian kernel. In this

study, the SSBIN-based feature with KPCA-G and using SVM-RBF is regarded as the proposed method, which is briefly denoted as the SSBIN method.

Finally, we listed MC_ACCs, MC_Ses, and MC_Sps of the SSBIN method on AD-vs-HC, AD-vs-MCI, MCI-vs-HC, and MCIc-vs-MCInc data sets in Table 3 under the cases of the directional level $S=3$, the decomposition scale $L=1$, the number of principal components $P=19$, the width of the Gaussian Kernel $K_W=2.3$, the window width of the RBF kernel $\sigma=2.2$, and the penalty coefficient of the SVM classifier $C=2$. As shown in Table 3, MC_ACCs of the SSBIN method are 94.78% on the AD-vs-HC data set, 90.00% on the AD-vs-MCI data set, 89.71% on the MCI-vs-HC data set, and 79.67% on the MCIc-vs-MCInc data set; MC_Ses of the SSBIN method on the AD-vs-HC and MCI-vs-HC data sets are superior to its MC_Ses, while MC_Ses of the SSBIN method are inferior to its MC_Sps on the AD-vs-MCI and MCIc-vs-MCInc data sets. The reason is that subjects with MCIc have more AD-like brain atrophy patterns; however, subjects with MCInc have more HC-like brain atrophy patterns, and meanwhile brain atrophies of HC individuals are slow and different from patients with AD and MCI. AUCs of the SSBIN method are 0.9875 on the AD-vs-HC data set, 0.9089 on the AD-vs-MCI data set, 0.9375 on the MCI-vs-HC data set and 0.8854 on the MCIc-vs-MCInc

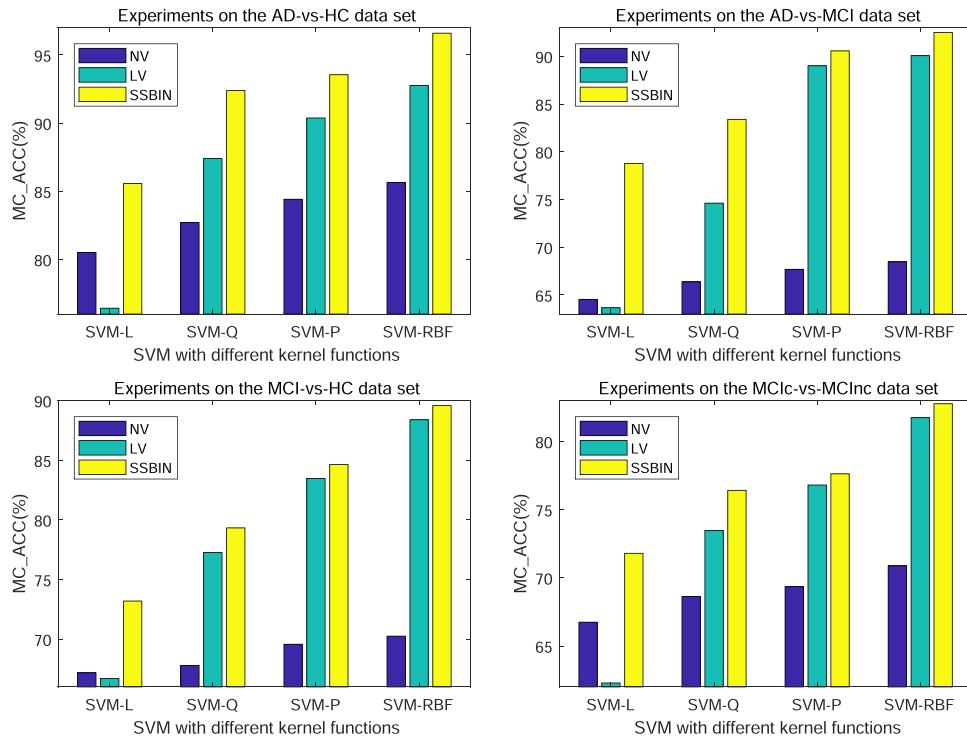


Fig. 10. MC_ACCs of AD detecting experiments using the LV, the NV, and the SSBIN-based feature on AD-vs-HC, AD-vs-MCI, MCI-vs-HC, and MCIc-vs-MCInc data sets.

Table 3

Experimental results of the SSBIN method on AD-vs-HC, AD-vs-MCI, MCI-vs-HC, and MCIc-vs-MCInc data sets under the cases of the directional level $S=3$, the decomposition scale $L=1$, the number of principal components $P=19$, the width of the Gaussian Kernel $K_W=2.3$, the window width of the RBF kernel $\sigma=2.2$, and the penalty coefficient of the SVM classifier $C=2$.

Four datasets	AD-vs-HC	AD-vs-MCI	MCI-vs-HC	MCIc-vs-MCInc
MC_ACC (%)	94.78	90.00	89.71	79.67
MC_Se (%)	96.94	88.30	91.18	78.30
MC_Sp (%)	91.20	91.70	87.65	81.05
AUC	0.9875	0.9089	0.9375	0.8854

data set. Results in Table 3 indicate that the SSBIN-based feature can represent the sMRI image properly.

On the whole, experimental results validate that the ROI can be properly described by the frequency domain-based feature, NV of the SSBIN can accurately describe the abnormal energy distribution patterns reflected in ROI, LV of the SSBIN is properly reconstructed by the KPCA with the Gaussian kernel, and the NV and the LV are complementary with each other in AD detection.

4. Comparison

In this section, we will compare the SSBIN method with four state-of-the-art approaches on AD-vs-HC, AD-vs-MCI, MCI-vs-HC, and MCIc-vs-MCInc data sets, including the hippocampal-based feature approach (HippF) (Li et al., 2019), the wavelet transform energy-based feature approach (WTEF) (Feng et al., 2020), the stationary wavelet entropy-based feature approach (SWEF) (Zhang et al., 2018), and the nonsubsample contourlet subband individual network-based feature approach (NCSIN) (Feng et al., 2021).

For the AD-vs-HC data set, experimental results of the four state-of-the-art comparison approaches and the SSBIN method are listed in Table 4. According to MC_ACCs, MC_Ses, MC_Sps and AUCs shown in Table 4, MC_ACC, MC_Se and AUC of the SSBIN method are consistently

Table 4

Experimental results of the four other state-of-the-art comparison approaches and the SSBIN method on the AD-vs-HC data set.

Method	MC_ACC (%)	MC_Se (%)	MC_Sp (%)	AUC
HippF (2019)	87.51	87.60	87.42	0.8450
WTEF (2020)	92.83	93.07	92.65	0.8850
SWEF (2018)	92.70	93.67	91.77	0.9325
NCSIN (2021)	94.21	96.58	92.44	0.9850
SSBIN	94.78	96.94	91.20	0.9875

higher than those of the four state-of-the-art comparison approaches; MC_ACC of the SSBIN method has reached to 94.78% and is marginally higher than that of the best comparison approach, MC_Se of the SSBIN method is 96.94% and is 0.36% higher than that of the best comparison approach, and AUC of the SSBIN method has reached to 0.9875. However, MC_Sp of the SSBIN method is 1.45% lower than that of the best comparison approach, which is 91.20%, the reason of which is that with aging, brain of the HC individual also gradually shrinks, whereas the SSBIN method can capture brain atrophy patterns by subbands, so the older HC subjects maybe identified as AD patients to a large extent. Experimental results on the AD-vs-HC data set validate that the ROI can be properly described by features extracted from the subband in the frequency domain, the NV extracted from the directional subbands can accurately describe those abnormal energy distribution patterns, and the LV extracted from these edge weights is properly reconstructed by the KPCA with the Gaussian kernel.

For the AD-vs-MCI data set, experimental results of the four state-of-the-art comparison approaches and the SSBIN method are listed in Table 5. It can be obviously seen from Table 5 that MC_Sp and AUC of the SSBIN method consistently outperforms those of the four state-of-the-art comparison approaches. MC_Sp of the SSBIN method is 91.70% and is 2.17% higher than that of the best comparison approach, and AUC of the SSBIN method has reached to 0.9089. But MC_ACC of the SSBIN method is 90.00%, which is marginally lower than that of the best comparison approach, and MC_Se of the SSBIN method is 2.70% lower than that of

Table 5

Experimental results of the four other state-of-the-art comparison approaches and the SSBIN method on the AD-vs-MCI data set.

Method	MC_ACC (%)	MC_Se (%)	MC_Sp (%)	AUC
HippF (2019)	79.35	79.44	79.26	0.7768
WTEF (2020)	84.40	80.11	87.91	0.7732
SWEF (2018)	81.89	76.26	80.65	0.7464
NCSIN (2021)	90.03	91.00	89.53	0.9018
SSBIN	90.00	88.30	91.70	0.9089

the four state-of-the-art comparison approaches, which is 88.30%. Experimental results on the AD-vs-MCI data set indicate that differences between atrophy patterns from patients with AD and MCI are small, resulting that patients with MCI are easily identified as AD. Therefore, MC_ACC and MC_Se of the SSBIN method is marginally poor. But this indirectly validates that atrophy patterns of the ROIs and correlations between them can be captured by the SSBIN-based feature.

For the MCI-vs-HC data set, experimental results of the four state-of-the-art comparison approaches and the SSBIN method are listed in Table 6. According to MC_ACCs, MC_Ses, MC_Sps and AUCs shown in Table 6, MC_ACC, MC_Sp and AUC of the SSBIN method are consistently higher than those of the four state-of-the-art comparison approaches, MC_ACC of the SSBIN method has reached to 89.71% and is 5.07% higher than that of the best comparison approach, MC_Sp of the SSBIN method is 0.67% higher than that of the best comparison approach, which is 87.65%, and AUC of the SSBIN method has reached to 0.9375. However, MC_Se of the SSBIN method is 91.18% and is 4.61% lower than that of the best comparison approach. Based on MC_ACCs of the SSBIN method shown in Tables 5 and 6, we can find that patients with MCI have more HC-like and in contrast less AD-like energy distribution patterns in their sMRI images, that is, brain tissues from patients with MCI are only partly destroyed to a small extent and this is the best time to benefit from the clinical treatment. Therefore, MCI is a key stage for the progression of a patient and identification of patients with MCI can make significant sense in clinics. Experimental results on the MCI-vs-HC data set show that differences between subjects with MCI and HC can be captured by the SSBIN-based feature, which means that correlations contained in different ROIs can be constructed by PCC using the subband energy feature in the frequency domain.

For the challenging MCIC-vs-MCInc data set, experimental results of the four state-of-the-art comparison approaches and the SSBIN method are listed in Table 7. It can be clearly observed from Table 7 that MC_ACC, MC_Sp and AUC of the SSBIN method consistently outperform those of the four state-of-the-art comparison approaches. MC_ACC of the SSBIN method is 79.67%, which is higher than 79.42% of the best comparison approach. MC_Sp of the SSBIN method is 81.05% and is 4.50% higher than that of the best comparison approach. AUC of the SSBIN method has reached to 0.8854. However, MC_Se of the SSBIN method is 4.00% lower than that of the best comparison approach, which is 78.30%. Experimental results on the MCIC-vs-MCInc data set further validate that differences between atrophy patterns of subjects with MCIC and MCInc can be captured by the SSBIN-based feature, the NV can accurately describe those abnormal energy distribution patterns contained in different ROIs, and the LV can be used to describe correlations between those ROIs.

Table 6

Experimental results of the four other state-of-the-art comparison approaches and the SSBIN method on the MCI-vs-HC data set.

Method	MC_ACC (%)	MC_Se (%)	MC_Sp (%)	AUC
HippF (2019)	77.25	95.79	53.23	0.8143
WTEF (2020)	80.82	76.49	85.70	0.8554
SWEF (2018)	80.67	76.79	86.98	0.8500
NCSIN (2021)	84.64	88.61	81.70	0.9125
SSBIN	89.71	91.18	87.65	0.9375

Table 7

Experimental results of the four other state-of-the-art comparison approaches and the SSBIN method on the MCIC-vs-MCInc data set.

Method	MC_ACC (%)	MC_Se (%)	MC_Sp (%)	AUC
HippF (2019)	69.38	69.47	69.29	0.7031
WTEF (2020)	73.43	70.06	75.59	0.7240
SWEF (2018)	72.86	69.55	75.49	0.6972
NCSIN (2021)	79.42	82.30	76.55	0.8542
SSBIN	79.67	78.30	81.05	0.8854

In order to make a visual comparison, ROC curves of the four comparison approaches and the SSBIN method on AD-vs-HC, AD-vs-MCI, MCI-vs-HC, and MCIC-vs-MCInc data sets are also given, which are shown in Fig. 11. It can be obviously seen from Fig. 11 that ROC curves of the SSBIN method on the four data sets are in the upper left corner, which further indicate that the SSBIN method outperforms the four state-of-the-art approaches.

In addition, we also give the mean computing time (MCT, in seconds) of the SSBIN method on MCIC/MCInc data set in identifying 160 subjects. The program runs on Matlab R2017a and computer with Intel(R) Core(TM) i7-4700 3.40 GHz CPU 64 bit system. Experimental results indicate that MCT of performing the shearlet transform on the GM image is 2.90 s, MCT of constructing the SSBIN feature is 0.50 s, and MCT of extracting the SSBIN feature from the GM image is 3.41 s. Obviously, the shearlet transform is time-consuming in the SSBIN method. While in comparison with the method HippF's 83.02 s, WTEF's 5.41 s, SWEF's 8.46 s, and NCSIN's 4.30 s, 3.41 s of the SSBIN method is more efficient.

Recently, the machine learning-based approach, especially the deep learning-based method, has been widely used in many fields. Therefore, we also compare the SSBIN method with the machine learning-based approaches, including the conventional learning-based approaches (DMTFS (Ye et al., 2016), LBFE (Zhang et al., 2016), and MKMFA (Cao et al., 2017)) and the deep learning-based approaches (DLASAE (Liu et al., 2014), VGGNet (Simonyan and Zisserman, 2015), and DenseNet (Liu et al., 2020)). Experimental results of the SSBIN method and published results of the machine learning-based approaches on AD-vs-HC and MCI-vs-HC data sets are listed in Table 8, respectively, including accuracy (ACC), sensitivity (Se) and specificity (Sp). According to Table 8, it can be seen that MC ACC, MC Se, MC Sp of the SSBIN method consistently outperform those of the machine learning-based approaches. The reason is two-fold. One is that for the deep learning-based methods, the input layer contains more than ten thousand nodes because of the high dimensionality of the sMRI image, which causes a huge number of parameters to deep learning framework, but samples can be used to train network architecture are small (Feng et al., 2021). Another is that the sMRI image contains a lot of redundant information such as the black background; therefore, the useful information may not be dominant in the extracted deep learning-based feature (Feng et al., 2021).

In summary, comprehensive comparisons validate the feasibility of representing ROI by directional subbands in the frequency domain, and demonstrate that the SSBIN method outperforms the four other state-of-the-art approaches in terms of MC ACC, MC Se, MC Sp, AUC and ROC, which indicates that the SSBIN-based feature can be an assistant imaging marker for the clinical AD diagnosis using the sMRI image.

5. Conclusions

In order to represent ROIs of the sMRI image in the frequency domain and then construct an individual network, in this study, a novel method is proposed to construct a SSBIN-based feature for detecting AD patients. Particularly, the shearlet transform is separately performed on each of the 90 ROIs to get the directional subband, following that a SSBIN is constructed with the 90 SVs and its weight values are calculated by PCC. Subsequently, we extract two features from the SSBIN, the NV is

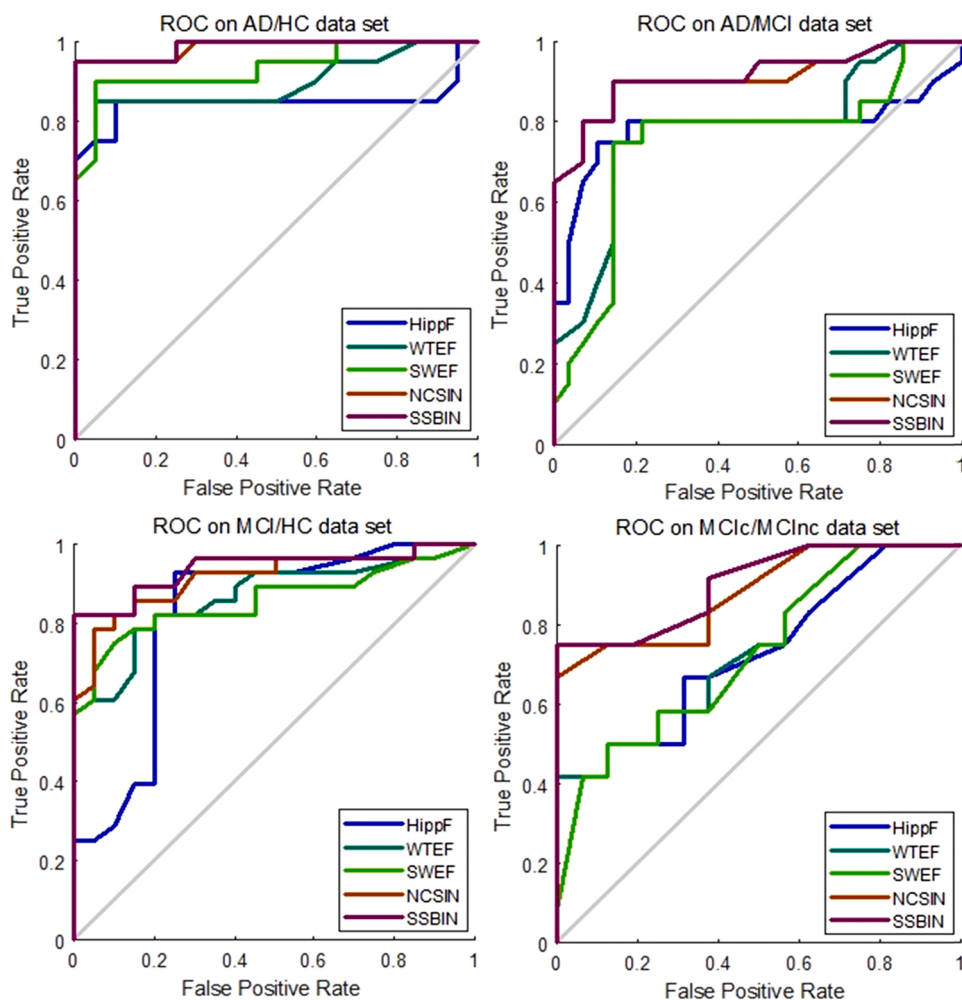


Fig. 11. ROC curves of the four comparison approaches and the SSBIN method on AD-vs-HC, AD-vs-MCI, MCI-vs-HC, and MCIc-vs-MCInc data sets.

Table 8

Results of the SSBIN method and those published of the machine learning-based approaches on AD-vs-HC and MCI-vs-HC data sets.

Method	AD/MCI/HC	AD-vs-HC (%)			MCI-vs-HC (%)		
		ACC	Se	Sp	ACC	Se	Sp
DMTFS	51/99/52	87.30	88.40	86.20	68.20	76.90	51.10
LBFE	51/99/52	83.10	80.50	85.10	73.60	75.30	69.70
MKMFA	192/397/229	88.60	85.70	90.40	71.90	79.00	60.70
DLASAE	65/169/77	87.80	88.60	87.20	76.92	74.29	78.13
VGGNet	97/233/119	84.70	77.30	90.80	70.90	81.90	65.20
DenseNet	97/233/119	88.90	86.60	90.80	76.20	79.50	69.80
SSBIN	200/280/200	94.78	96.94	96.20	89.71	91.18	87.65

computed by averaging these SVs, and the LV is obtained by KPCA. Finally, concatenation of the NV and the LV is used as the SSBIN-based feature. Even though the SSBIN method can achieve a better AD detecting performance, features extracted from the SSBIN are not associated with the genetic information related to AD. In addition, sMRI is not the only modality for AD diagnosis. Hence more clinical information should be considered to make an accurate AD detection. Therefore, in the future work, we will extract features from the combination of multiple modalities for AD detection.

Declaration of Competing Interest

The authors declare that they have no known competing financial interests or personal relationships that could have appeared to influence the work reported in this paper.

Acknowledgment

This paper was supported by the National Natural Science Foundation of China (Grant Nos. 61873202, 61473232, 91430111, 12131020, 31930022, 12026608, 81471047, 31930022, 120266088 and 11871456), National Key R&D Program (Grant Nos. 2017YFA0505500 and 2016YFC0903400), Strategic Priority Research Program of the Chinese Academy of Sciences (Grant No. XDB38040400), and Natural Science Foundation of Shanghai (Grant No. 17ZR1446100).

We also thank the ADNI very much for their data collection and sharing. For more information, we refer readers to website of the ADNI: adni.loni.usc.edu.

CRedit author statement

Feng Jinwang: Conceptualization, Methodology, Software, Writing – Original draft preparation. Zhang Shao-Wu and Chen Luonan: Writing – review & editing, Supervision, Funding acquisition. Zuo Chunman: Data Curation, Writing – review & editing.

References

- Alzheimer's Association, 2018. Alzheimer's association report: 2018 Alzheimer's disease facts and figures. *Alzheimer's Dement.* 14, 367–429. <https://doi.org/10.1016/j.jalz.2018.02.001>.
- Arbabshirani, M.R., Plis, S., Sui, J., Calhoun, V.D., 2017. Single subject prediction of brain disorders in neuroimaging: promises and pitfalls. *Neuroimage* 145, 137–165. <https://doi.org/10.1016/j.neuroimage.2016.02.079>.
- Ardekani, B.A., Bermudez, E., Mubeen, A.M., Bachman, A.H., 2017. Prediction of incipient Alzheimer's disease dementia in patients with mild cognitive impairment. *J. Alzheimer's Dis.* 55, 269–281. <https://content.iospress.com/articles/journal-of-alzheimers-disease/jad160594>.
- Ashburner, J., Friston, K.J., 2000. Voxel-based morphometry—the methods. *Neuroimage* 11, 805–821. <https://doi.org/10.1006/nimg.2000.0582>.
- Ashburner, J., Friston, K., Holmes, A., Poline, J.-B., 1994. Statistical Parametric Mapping (SPM8), The Wellcome Dept. Cognitive Neurology, Univ. College London, London, U.K. Available: <http://www.fil.ion.ucl.ac.uk/spm/>.
- Beheshti, I., Demirel, H., Farokhian, F., Yang, C., Matsuda, H., 2016. Structural MRI-based detection of Alzheimer's disease using feature ranking and classification error. *Comput. Methods Prog. Biomed.* 137, 177–193. <https://doi.org/10.1016/j.cmpb.2016.09.019>.
- Cao, P., Liu, X., Yang, J., Zhao, D., Huang, M., Zhang, J., Zaiane, O., 2017. Nonlinearity-aware based dimensionality reduction and over-sampling for AD/MCI classification from MRI measures. *Comput. Biol. Med.* 91, 21–37. <https://doi.org/10.1016/j.combiomed.2017.10.002>.
- Cao, P., Shan, X., Zhao, D., Huang, M., Zaiane, O., 2017. Sparse shared structure based multi-task learning for MRI based cognitive performance prediction of Alzheimer's disease. *Pattern Recognit.* 72, 219–235. <https://doi.org/10.1016/j.patcog.2017.07.018>.
- Cevik, A., Weber, G.W., Evuboglu, B.M., Oguz, K.K., 2017. Voxel-MARS: A method for early detection of Alzheimer's disease by classification of structural brain MRI. *Ann. Oper. Res.* 258, 31–57. <https://doi.org/10.1007/s10479-017-2405-7>.
- Cheng, B., Liu, M., Zhang, D., Shen, D., 2019. Robust multi-label transfer feature learning for early diagnosis of Alzheimer's disease. *Brain Imag. Behav.* 13, 138–153. <https://linkspringer.53yu.com/article/10.1007/s11682-018-9846-8>.
- Coronado-Leija, R., Ramirez-Manzanares, A., Marroquin, J.L., 2017. Estimation of individual axon bundle properties by a multi-resolution discrete-search method. *Med. Image Anal.* 42, 26–43. <https://doi.org/10.1016/j.media.2017.06.008>.
- Cuingnet, R., Gerardin, E., Tessieras, J., Auzias, G., Lehericy, S., Habert, M.O., Chupin, M., Benali, H., Colliot, O., 2011. Automatic classification of patients with Alzheimer's disease from structural MRI: a comparison of ten methods using the ADNI database. *Neuroimage* 56, 766–781. <https://doi.org/10.1016/j.neuroimage.2010.06.013>.
- Cunha, A.L., Zhou, J., Do, M.N., 2006. The nonsubsampled contourlet transform: theory, design, and applications. *IEEE Trans. Image Process.* 15, 3089–3100. <https://ieeexploreieee.53yu.com/abstract/document/1703596>.
- Dai, T., Guo, Y., 2017. Alzheimer's disease neuroimaging initiative: predicting individual brain functional connectivity using a Bayesian hierarchical model. *Neuroimage* 147, 772–787. <https://doi.org/10.1016/j.neuroimage.2016.11.048>.
- Do, M.N., Vetterli, M., 2005. The contourlet transform: an efficient directional multiresolution image representation. *IEEE Trans. Image Process.* 14, 2091–2106. <https://ieeexploreieee.53yu.com/abstract/document/1532309>.
- Dong, Y., Tao, D., Li, X., Ma, J., Pu, J., 2015. Texture classification and retrieval using shearlet and linear regression. *IEEE Trans. Cyber.* 45, 358–369. <https://ieeexploreieee.53yu.com/abstract/document/6853375>.
- Dong, Y., Feng, J., Liang, L., Zheng, L., Wu, Q., 2017. Multiscale sampling based texture image classification. *IEEE Signal Process. Lett.* 24, 614–618. <https://ieeexploreieee.53yu.com/abstract/document/7857682>.
- Duraisamy, B., Shanmugam, J.V., Annamalai, J., 2019. Alzheimer disease detection from structural MR images using FCM based weighted probabilistic neural network. *Brain Imag. Behav.* 13, 87–110. <https://doi.org/10.1007/s11682-018-9831-2>.
- Easley, G., Labate, D., Lim, W.Q., 2008. Sparse directional image representations using the discrete shearlet transform. *Appl. Comput. Harmon. A* 25, 25–46. <https://doi.org/10.1016/j.acha.2007.09.003>.
- El-Yacoubi, M.A., Garcia-Salicetti, S., Kahindo, C., Rigaud, A.S., Cristancho-Lacroix, V., 2019. From aging to early-stage Alzheimer's: uncovering handwriting multimodal behaviours by semi-supervised learning and sequential representation learning. *Pattern Recognit.* 86, 112–133. <https://doi.org/10.1016/j.patcog.2018.07.029>.
- Farrar, D.C., Mian, A.Z., Budson, A.E., Moss, M.B., Koo, B.B., Killiany, R.J., 2018. Retained executive abilities in mild cognitive impairment are associated with increased white matter network connectivity. *Eur. Radiol.* 28, 340–347. <https://linkspringer.53yu.com/article/10.1007/s00330-017-4951-4>.
- Feng, J., Liu, X., Dong, Y., Liang, L., Pu, J., 2016. Structural difference histogram representation for texture image classification. *IET Image Process.* 11, 118–125. https://www.researchgate.net/publication/309144790_Structural_Difference_Histogram_Representation_for_Texture_Image_Classification.
- Feng, J., Zhang, S.W., Chen, L., 2020. Identification of Alzheimer's disease based on wavelet transformation energy feature of the structural MRI image and NN classifier. *Artif. Intell. Med.* 108, 101940. <https://doi.org/10.1016/j.artmed.2020.101940>.
- Feng, J., Zhang, S.W., Chen, L., 2021. Extracting ROI-based contourlet subband energy feature from the sMRI image for Alzheimer's disease classification. *IEEE/ACM Trans. Comput. Biol. Bioinf.* Doi:10.1109/TCBB.2021.3051177. <https://ieeexploreieee.53yu.com/abstract/document/9320583>.
- Feng, J., Zhang, S.W., Chen, L., Xia, J., 2021. Alzheimer's disease classification using features extracted from nonsubsampled contourlet subband-based individual networks. *Neurocom* 421, 160–273. <https://doi.org/10.1016/j.neucom.2020.09.012>.
- Giulietti, G., Torso, M., Serra, L., Spano, B., MD C. M., MD C. C., Cercignani, M., MD M. B., 2018. Whole brain white matter histogram analysis of diffusion tensor imaging data detects microstructural damage in mild cognitive impairment and Alzheimer's disease patients. *J. Magn. Reson. Imag.* 48, 767–779. <https://doi.org/10.1002/jmri.25947>.
- Glozman, T., Solomon, J., Pestilli, F., Guibas, L., 2017. Shape-attributes of brain structures as biomarkers for Alzheimer's disease. *J. Alzheimer's Dis.* 56, 287–295. <https://content.iospress.com/articles/journal-of-alzheimers-disease/jad160900>.
- Guo, Z., Xiong, H., Liu, X., Zhang, H., Ghista, D., Wu, W., 2017. Robust estimation of carotid artery wall motion using the elasticity-based state-space approach. *Med. Image Anal.* 37, 1–21. <https://doi.org/10.1016/j.media.2017.01.004>.
- Jha, D., Alam, S., Pyun, J.Y., Lee, K.H., Kwon, G.R., 2018. Alzheimer's disease detection using extreme learning machine, complex dual tree wavelet principal coefficients and linear discriminant analysis. *J. Med. Imag. Health Inf.* 8, 881–890. <https://doi.org/10.1166/jmih.2018.2381>.
- Ju, R., Hu, C., Zhou, P., Li, Q., 2019. Early diagnosis of Alzheimer's disease based on resting-state brain networks and deep learning. *IEEE/ACM Trans. Comput. Biol. Bioinf.* 16, 244–257. <https://ieeexploreieee.53yu.com/abstract/document/8119531>.
- Lee, J.M., Yoo, C.K., Choi, S.W., Vanrolleghem, P.A., Lee, I.B., 2004. Nonlinear process monitoring using kernel principal component analysis. *Chem. Eng. Sci.* 59, 223–234. <https://doi.org/10.1016/j.ces.2003.09.012>.
- Li, H., Habes, M., Wolk, D.A., Fan, Y., 2019. A deep learning model for early prediction of Alzheimer's disease dementia based on hippocampal magnetic resonance imaging data. *Alzheimer's Dement.* 15, 139–150. <https://doi.org/10.1016/j.jalz.2019.02.007>.
- Liu, J., Wang, J., Hu, B., Wu, F.X., Pan, Y., 2017. Alzheimer's disease classification based on individual hierarchical networks constructed with 3-D texture features. *IEEE Trans. Nanobiosci.* 16, 428–437. <https://ieeexploreieee.53yu.com/abstract/document/7932999>.
- Liu, J., Li, M., Lan, W., Wu, F.X., Wang, J., 2018. Classification of Alzheimer's disease using whole brain hierarchical network. *IEEE/ACM Trans. Comput. Biol. Bioinf.* 55, 624–632. <https://ieeexploreieee.53yu.com/abstract/document/7765123>.
- Liu, M., Zhang, D., Adeli, E., Shen, D., 2015. Inherent structure-based multiview learning with multitemplate feature representation for Alzheimer's disease diagnosis. *IEEE Trans. Biomed. Eng.* 63, 1473–1482. <https://ieeexploreieee.53yu.com/abstract/document/7312947>.
- Liu, M., Zhang, J., Nie, D., Yap, P.T., Shen, D., 2018. Anatomical landmark based deep feature representation for MR images in brain disease diagnosis. *IEEE J. Biomed. Health Inform.* 22, 1476–1485. <https://ieeexploreieee.53yu.com/abstract/document/8253440>.
- Liu, M., Li, F., Yan, H., Wang, K., Ma, Y., Shen, L., Xu, M., 2020. A multi-model deep convolutional neural network for automatic hippocampus segmentation and classification in Alzheimer's disease. *NeuroImage* 208, 116459. <https://doi.org/10.1016/j.neuroimage.2019.116459>.
- Liu S., Liu S., Cai W., Pujol S., Kikinis R., Feng D., 2014. Early diagnosis of Alzheimer's disease with deep learning. 2014 In: Proceedings of the IEEE 11th ISBI, IEEE, Beijing, pp. 1015–1018. <https://ieeexploreieee.53yu.com/abstract/document/6868045>.
- Long, X., Chen, L., Jiang, C., Zhang, L., 2017. Prediction and classification of Alzheimer disease based on quantification of MRI deformation. *PLOS One* 12, e0173372–e0173390. <https://journals.plos.org/plosone/article?id=10.1371/journal.pone.0173372>.
- Lu, D., Popuri, K., Ding, G.W., Balachandrar, R., Beg, M.F., 2018. Multimodal and multiscale deep neural networks for the early diagnosis of Alzheimer's disease using structural MR and FDG-PET images. *Sci. Rep.* 8, 5697–5709. <https://doi.org/10.1038/s41598-018-22871-z>.
- Moetesum, M., Siddiqi, I., Vincent, N., Cloppet, F., 2019. Assessing visual attributes of handwriting for prediction of neurological disorders – a case study on Parkinson's disease. *Pattern Recognit. Lett.* 121, 19–27. <https://doi.org/10.1016/j.patrec.2018.04.008>.
- Ou, J., Xie, L., Li, X., Zhu, D., Terry, D.P., Puente, A.N., Jiang, R., Chen, Y., Wang, L., Shen, D., Zhang, J., Miller, L.S., Liu, T., 2015. Atomic connectomics signatures for characterization and differentiation of mild cognitive impairment. *Brain Imaging Behav.* 9, 663–677. <https://doi.org/10.1007/s11682-014-9320-1>.
- Partovi, S., Yuh, R., Pirozzi, S., Lu, Z., Couturier, S., Grosse, U., Schluchter, M., Nelson, A., Jones, R., O'Donnell, J., Faulhaber, P., 2017. Diagnostic performance of an automated analysis software for the diagnosis of Alzheimer's dementia with 18F FDG PET. *American J. Nucl. Med. Mol. Imaging* 7, 12–23. https://www.researchgate.net/publication/312973290_Diagnostic_performance_of_an_automated_analysis_software_for_the_diagnosis_of_Alzheimer's_dementia_with_18F_FDG_PET.
- Peng, J., Zhu, X., Wang, Y., An, L., Shen, D., 2019. Structured sparsity regularized multiple kernel learning for Alzheimer's disease diagnosis. *Pattern Recognit.* 88, 370–382. <https://doi.org/10.1016/j.patcog.2018.11.027>.
- Romdhani S., Gong S., Psarrour A., 1999. A multi-view nonlinear active shape model using kernel PCA. In: Proceedings of the British Machine Vision Conference, pp. 13–16. https://www.researchgate.net/publication/2852288_A_Multi-View_Nonlinear_Active_Shape_Model.
- Saravanakumar, S., Thangaraj, P., 2019. A voxel based morphometry approach for identifying Alzheimer from MRI images. *Clust. Comput.* 22, 14081–14089. <https://doi.org/10.1007/s10586-018-2236-6>.
- Scholkopf B., Smola A., Muller K.R., 1997. Kernel principal component analysis. In: Proceedings of the International Conference on Artificial Neural Networks 1327, pp. 583–588. <https://doi.org/10.1007/BFb0020217>.

- Shachar, N., Mitelpunkt, A., Kozlovski, T., Galili, T., Frostig, T., Brill, B., Marcus-Kalish, M., Benjamini, Y., 2018. The importance of non-linear transformations uses in medical data analysis. *JMIR Med. Inf.* 6, e27–e35. (<https://medinform.jmir.org/2018/2/e27>).
- Simonyan K., Zisserman A., 2015. Very deep convolutional networks for large scale image recognition. In: *Proceedings of the International Conference on Learning Representations (ICLR)*. (<https://arxiv.53yu.com/abs/1409.1556>).
- Stefano, C.D., Fontanella, F., Impedovo, D., Pirlo, G., Freca, A.S.D., 2019. Hand-writing analysis to support neurodegenerative disease diagnosis: a review. *Pattern Recognit.* 121, 37–45. (<https://doi.org/10.1016/j.patrec.2018.05.013>).
- Suk, H.I., Lee, S.W., Shen, D., 2015. Latent feature representation with stacked auto-encoder for AD/MCI diagnosis. *Brain Struct. Funct.* 220, 841–859. (<https://linkspringer.53yu.com/article/10.1007/s00429-013-0687-3>).
- Swietlik, D., Bialowas, J., 2019. Application of artificial neural networks to identify Alzheimer's disease using cerebral perfusion SPECT data. *Int. J. Environ. Res. Public Health* 16, 1303–1311. (<https://doi.org/10.3390/ijerph16071303>).
- Thung, K.H., Yap, P.T., Adeli, E., Lee, S.W., Shen, D., 2018. Conversion and time-to-conversion predictions of mild cognitive impairment using low-rank affinity pursuit denosing and matrix completion. *Med. Image Anal.* 45, 68–82. (<https://doi.org/10.1016/j.media.2018.01.002>).
- Tzourio-Mazoyer, N., Landeau, B., Papathanassiou, D., Crivello, F., Etard, O., Delcroix, N., Mazoyer, B., Joliot, M., 2002. Automated anatomical labelling of activations in SPM using a macroscopic anatomical parcellation of the MNI MRI single-subject brain. *NeuroImage* 15, 273–289. (<https://doi.org/10.1006/nimg.2001.0978>).
- Vogel, J.W., Vachon-Preseau, E., Binette, A.P., Tam, A., Orban, P., Joie, R.L., Savard, M., Picard, C., Poirier, J., Bellec, P., Breitner, J.C.S., Villeneuve, S., 2018. Brain properties predict proximity to symptom onset in sporadic Alzheimer's disease. *Brain* 141, 1871–1883. (<https://doi.org/10.1093/brain/awy093>).
- Wang, Z., Zhu, X., Adeli, E., Zhu, Y., Nie, F., Munsell, B., Wu, G., 2017. Multi-modal classification of neurodegenerative disease by progressive graph-based transductive learning. *Med. Image Anal.* 39, 218–230. (<https://doi.org/10.1016/j.media.2017.05.003>).
- Wiepert, A.D., Lowe, V.J., Knopman, D.S., Boeve, B.F., Graff-Radford, J., Petersen, R.C., Jack Jr., C.R., Jones, D.T., 2017. A robust biomarker of large-scale network failure in Alzheimer's disease. *Alzheimer's Dement. Diagn. Assess. Dis. Monit.* 6, 152–161. (<https://doi.org/10.1016/j.dadm.2017.01.004>).
- Ye, T., Zu, C., Jie, B., Shen, D., Zhang, D., 2016. Discriminative multi-task feature selection for multi-modality classification of Alzheimer's disease. *Brain Imaging Behav.* 10, 739–749. (<https://doi.org/10.1007/s11682-015-9437-x>).
- Zhang, J., Gao, Y., Gao, Y., Munsell, B.C., Shen, D., 2016. Detecting anatomical landmarks for fast Alzheimer's disease diagnosis. *IEEE Trans. Med. Imaging* 35, 2524–2533. (<https://ieeexploreieee.53yu.com/abstract/document/7494619>).
- Zhang, M., Golland, I.I.I.W.M.W., P., 2017. Probabilistic modelling of anatomical variability using a low dimensional parameterization of diffeomorphisms. *Med. Imag. Anal.* 41, 55–62. (<https://doi.org/10.1016/j.media.2017.06.013>).
- Zhang, Y., Wang, S., Sui, Y., Yang, M., Liu, B., Cheng, H., Sun, J., Jia, W., Phillips, P., Gorriz, J.M., 2018. Multivariate approach for Alzheimer's disease detection using stationary wavelet entropy and predator-prey particle swarm optimization. *J. Alzheimer's Dis.* 65, 855–869. (<https://content.iospress.com/articles/journal-of-alzheimers-disease/jad170069>).
- Zhang, Y., Zhang, H., Chen, X., Liu, M., Zhu, X., Lee, S.W., Shen, D., 2019. Strength and similarity guided group-level brain functional network construction for MCI diagnosis. *Pattern Recogn.* 88, 421–430. (<https://doi.org/10.1016/j.patcog.2018.12.001>).
- Zhang, Y., Zhang, H., Adeli, E., Chen, X., Liu, M., Shen, D., 2020. Multiview feature learning with multiatlas-based functional connectivity networks for MCI diagnosis. *IEEE Trans. Cyber. Doi: 10.1109/TCYB.2020.3016953* (<https://ieeexplore.ieee.org/abstract/document/9292421>).
- Zhou, Q., Goryawala, M., Cabrerizo, M., Wang, J., Barker, W., Loewenstein, D.A., Duara, R., Adjouadi, M., 2014. An optimal decisional space for the classification of Alzheimer's disease and mild cognitive impairment. *IEEE Trans. Biomed. Eng.* 65, 2245–2253. (<https://ieeexploreieee.53yu.com/abstract/document/6762938>).
- Zhou, Z., Chen, X., Zhang, Y., Hu, D., Qiao, L., Yu, R., Yap, P.T., Pan, G., Zhang, H., Shen, D., 2020. A toolbox for brain network construction and classification (BrainNetClass). *Hum. Brain Mapp.* 41, 2808–2826. (<https://doi.org/10.1002/hbm.24979>).
- Zhu, X., Su, H.I. k, Lee, S.W., Shen, D., 2019. Discriminative self-representation sparse regression for neuroimaging-based alzheimer's disease diagnosis. *Brain Imag. Behav.* 13, 27–40. (<https://doi.org/10.1007/s11682-017-9731-x>).